Anthropogenic Forcing and Decadal Climate Variability in Sensitivity Experiments of Twentieth- and Twenty-First-Century Climate

GERALD A. MEEHL, WARREN M. WASHINGTON, JULIE M. ARBLASTER, THOMAS W. BETTGE, AND WARREN G. STRAND JR.

National Center for Atmospheric Research, Boulder, Colorado*

(Manuscript received 15 June 1998, in final form 26 January 2000)

ABSTRACT

A methodology is formulated to evaluate the possible changes in decadal-timescale (10–20-yr period) surface temperature variability and associated low-frequency fluctuations of anthropogenic forcing and changes in climate base state due to the forcing in simulations of twentieth- and twenty-first-century climate in a global coupled climate model without flux adjustment. The two climate change experiments both start in the year 1900. The first uses greenhouse gas radiative forcing (represented by equivalent CO_2) observed during the twentieth century, and extends greenhouse gas forcing to the year 2035 by increasing CO_2 1% yr^{-1} compound after 1990 (CO_2-only experiment). The second includes the same greenhouse gas forcing as the first, but adds the effects of time-varying geographic distributions of monthly sulfate aerosol radiative forcing represented by a change in surface albedo (CO_2 + sulfates experiment). The climate change experiments are compared with a 135-yr control experiment with no change in external forcing. Climate system responses in the CO_2-only and CO_2 + sulfates experiments in this particular model are marked not only by greater warming at high latitudes in the winter hemisphere, but also by a global El Niño–like pattern in surface temperature, precipitation, and sea level pressure. This pattern is characterized by a relatively greater increase of SST in the central and eastern equatorial Pacific in comparison with the west, a shift of precipitation maxima from the western Pacific to the central Pacific, mostly decreases of Asian–Australian monsoon strength, lower pressure over the eastern tropical Pacific, deeper midlatitude troughs in the North and South Pacific, and higher pressure over Australasia. Time series analysis of globally averaged temperature and an EOF analysis of surface temperature are consistent with previous results in that enhanced low-frequency variability with periods greater than around 20 yr is introduced into the model coupled climate system with a comparable timescale to the forcing. To examine the possible effects of the associated changes in base state on decadal timescale variability (10–20-yr periods), the surface temperature time series are filtered to retain only variability on that timescale. The El Niño–like pattern of decadal variability seen in the observations is present in each of the model experiments (control, CO_2 only, and CO_2 + sulfates), but the magnitude decreases significantly in the CO_2-only experiment. This decrease is associated with changes in the base-state climate that include a reduction in the magnitude (roughly 5%–20% or more) of wind stress and ocean currents in the upper 100 m in most ocean basins and a weakening of meridional overturning (about 50%) in the Atlantic. These weakened circulation features contribute to decreasing the amplitude of global decadal surface temperature variability as seen in a previous sea-ice sensitivity study with this model. Thus the superposition of low-frequency variability patterns in the radiative forcing increases climate variability for periods comparable to those of the forcing (greater than about 20 yr). However, there are decreases in the amplitude of future decadal (10–20-yr period) variability in these experiments due to changes of the base-state climate as a consequence of increases in that forcing.

1. Introduction

Since the mid-1990s, there have been a number of global coupled modeling studies that have included time-varying climate system forcings singly and from a combination of CO_2 and sulfate aerosols as single realizations (Mitchell et al. 1995a,b; Hasselmann et al. 1995; Meehl et al. 1996; Haywood et al. 1997; Hegerl et al. 1997; Mitchell and Johns 1997). Typically, the globally averaged response of the climate system depends on the magnitude of the forcing and responds in kind to time-varying fluctuations of that forcing (Wigley and Raper 1990). Additionally, the effects of the forcings appear to be additive to a first order (Meehl et al. 1996; Haywood et al. 1997).

By including combinations of anthropogenic forcings, there has been a more realistic assessment of the patterns produced by these forcings, in particular in the

* The National Center for Atmospheric Research is sponsored by the National Science Foundation

Corresponding author address: Dr. Gerald Meehl, NCAR, 1850 Table Mesa Drive, P.O. Box 3000, Boulder, CO 80307.
E-mail: meehl@ncar.ucar.edu

context of detection/attribution studies (Santer et al. 1996; Hegerl et al. 1997). One regional pattern of mean climate change due to increased CO_2 seen in some models (including the one in this paper) is the so-called El Niño–like pattern (Knutson and Manabe 1995, 1998; Tett 1995; Meehl and Washington 1996; Meehl et al. 1996; Timmermann et al. 1999). This is manifested as the mean climate change from an increase of atmospheric CO_2 whereby the eastern tropical Pacific warms faster than the western tropical Pacific, with attendant eastward shifts in precipitation. This type of mean climate change pattern, superimposed on interannual El Niño–Southern Oscillation (ENSO) and decadal variability with a similar pattern (Kang 1996; Zhang et al. 1997; Lau and Weng 1999), could result in potentially serious water resource impacts in the Pacific region (Meehl 1996). However, the El Niño–like response to increased CO_2 remains somewhat model dependent given that at least one global coupled model simulates a La Niña–like response (Noda et al. 1999). A comparison of a global coupled model that does not simulate an El Niño–like response, and the model in the current paper that does, shows that the nature of cloud feedbacks in the models contributes to such a response (Meehl et al. 2000b).

Single realizations (e.g., Meehl et al. 1993; Tett 1995; Knutson et al. 1997; Timmermann et al. 1999) and ensembles of climate change experiments (Collins 2000) have been analyzed to address possible future changes in interannual timescale variability associated with ENSO. Though not yet definitive, what is important about those studies is that they have recognized such possible changes could be important in the climate system and have proposed some mechanisms and methodologies to begin to study the problem.

Comparable changes to decadal timescale variability in the future have received less attention. It is generally assumed that the change in base state in a future climate or the low-frequency variability that is introduced into the climate system associated with the time-varying forcing does not affect decadal climate variability (Hegerl et al. 1997). Here we address the general question of how changes in the base state and introduced low-frequency variability could affect the manifestation of decadal variability in a global coupled climate model. As in most of the studies mentioned above concerning possible changes to ENSO variability in a future climate, there are issues of integration length or the need for ensembles in coming to definite conclusions on decadal variability changes. Yet it is important to recognize that such possible changes could be important in the climate system and to begin to address them.

The twentieth- and twenty-first-century climate experiments described here are single realizations from a global coupled climate model with CO_2 only and a combination of CO_2 and sulfate aerosol forcing from 1900 to 2035. Subsequent experiments are being run with improved model components and different forcing scenarios. Thus we treat these initial experiments as sensitivity studies for the purpose of first describing features associated with the twentieth- and twenty-first-century simulations to document the changes in the mean climate base state. Then a methodology will be described to analyze the effects of time-varying external forcing from changes in CO_2 and sulfate aerosols on decadal (10–20-yr period) climate variability in the model. This methodology could then be applied to subsequent longer integrations, stabilization experiments, or ensembles of climate change experiments. The changes in the mean state will turn out to be directly relevant to understanding the mechanism for changes in decadal variability.

This particular model has high sensitivity as compared with other models of its class (Kattenberg et al. 1996, Fig. 6.4 and Table 6.3), and does not use flux adjustment. Some aspects of the model associated with ice–albedo feedback and cloud feedbacks have been identified as contributing to this high sensitivity (Meehl et al. 2000b). The model also has a reasonably high resolution ocean model in comparison with other present global coupled models ($1^\circ \times 1^\circ$). The coupled model has been run in a series of sensitivity studies that were the first to include combinations of the direct and indirect effects of sulfate aerosol forcing in a global coupled GCM (Meehl et al. 1996). The current experiments follow those in terms of the specification of patterns of the monthly mean sulfate aerosol forcing, but include them in a real-time evolving sense.

First we will describe the model used in this study and the experimental design. Then basic features of surface temperature, sea level pressure (SLP), and precipitation changes will be presented. Last, EOF analyses of surface temperature will document the El Niño–like pattern related to the time evolution of the forcing, the decadal variability associated with this pattern, and the changes in decadal variability associated with the time-varying forcing and altered base state in the model.

2. Model and experiments

The global coupled climate model used in these experiments is referred to as the Department of Energy (DOE) global coupled model, which is the predecessor to the more recent DOE Parallel Climate Model. The model analyzed here, the DOE coupled model, has an atmospheric component with rhomboidal-15 (R15) resolution (roughly 4.5° lat $\times$ 7.5° long) with nine levels, mass flux convection, and a cloud albedo feedback scheme; a global $1^\circ \times 1^\circ$ 20-level ocean; and dynamic and thermodynamic sea ice (Meehl and Washington 1995; Washington and Meehl 1996). The model uses an initialization spinup from the observed ocean state (Levitus 1982).

Characteristics of this model are described by Meehl and Washington (1995) for sensitivity aspects of the cloud–albedo feedback scheme and some comparisons

of the model simulation features with observations. Meehl (1997) notes details on the spinup and systematic errors of SST and surface fluxes compared to observations. Washington and Meehl (1996) include a basic description of a 1% yr^{-1} CO_2 increase experiment and features of the high-latitude simulation in the model in comparison with observations as well as the response in the Northern Hemisphere to increasing CO_2. Meehl and Washington (1996) describe the El Niño–like SST response pattern in the 1% CO_2 increase sensitivity experiment, and Meehl et al. (1996) show results from a set of sensitivity experiments including the 1% yr^{-1} CO_2 increase experiment as compared with experiments that include direct and indirect effects of sulfate aerosols. Results from the coupled model 1% CO_2 increase sensitivity experiment appeared in the Second Assessment Report of the Intergovernmental Panel on Climate Change (IPCC; Houghton et al. 1996) where, as noted above, this particular model had high climate sensitivity (4.6°C for equilibrium response to doubled CO_2, 3.8°C at time of CO_2 doubling in the 1% per year transient CO_2 increase fully coupled experiment) in comparison with other models of its class for identifiable reasons (Meehl et al. 2000b). Additionally, unlike many other global coupled models that have low-amplitude decadal timescale variability (e.g., Capotondi and Holland 1999), this coupled model has relatively high amplitude decadal timescale variability (i.e., 10–20 yr) in comparison with observations (Meehl et al. 1998, 2000a).

The sensitivity experiments here follow the studies of Meehl et al. (1996). Those were future climate sensitivity integrations where a 1% compound CO_2 increase was combined with the direct effect of sulfate aerosol forcing (represented as a change in surface albedo), and inclusion of the direct plus indirect effect (the latter represented by a change in cloud albedo) of sulfate aerosols. The surface albedo change representation is one of three methods used in current models (the other two are prescribed time-evolving 3D sulfate aerosol concentrations, and time-evolving sulfur emissions used in conjunction with sulfur chemistry formulations). To a first order, the simpler scheme compares favorably with more detailed ones in terms of the large-scale aspects of the response given the uncertainties in the physics (Cubasch et al. 2000, to appear in *Climate Change 2000: The Science of Climate Change, the IPCC Third Assessment Report*, published by Cambridge University Press).

In addition to a 135-yr control experiment with no change in external forcing, we have performed two other integrations with the model starting in 1900, and the forcing scenarios are shown in Fig. 1a. In the first experiment (termed here "CO_2 only"), we specify observed, historical greenhouse gas forcing from 1900 to 1990 based on equivalent CO_2 computed in relation to preindustrial values derived from Houghton et al. (1990). After 1990, the greenhouse gas forcing is calculated from an increase of CO_2 at a rate of 1% yr^{-1} compound.

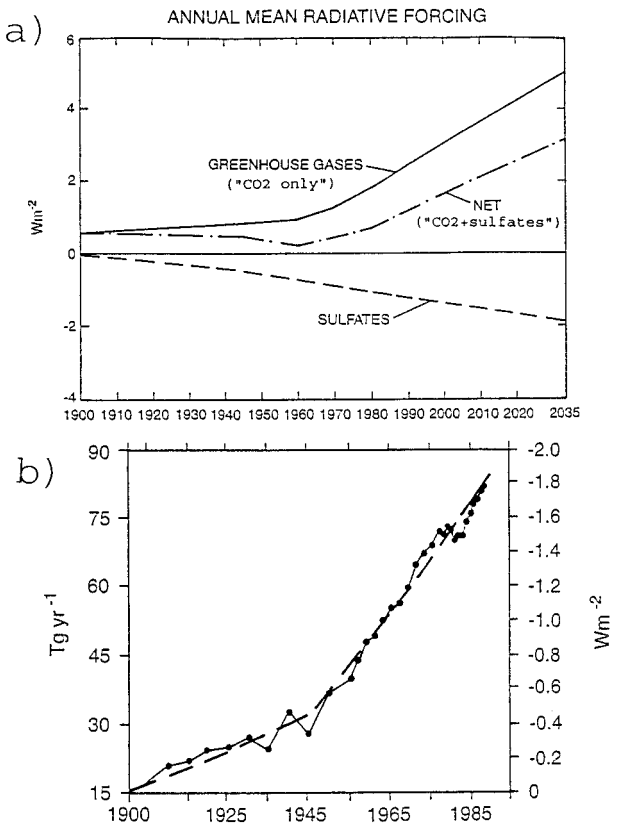

FIG. 1. (a) Time series of globally averaged annual mean radiative forcing (W m^{-2}) used in the anthropogenic climate change experiments as described in the text for the period 1900–2035 for greenhouse gases (solid line, equivalent CO_2 only, used for the CO_2-only experiment), sulfate aerosols (dashed), and "Net" for net radiative forcing from greenhouse gases plus sulfate aerosols (dot–dash, sum of solid and dashed lines in the figure, used for the "CO_2 + sulfates" experiment); (b) time series of sulfur dioxide emissions (Tg yr^{-1}) from Boden et al. (1994; dots connected by solid line), and radiative forcing fitted to the emissions (dashed line) for the period 1900–95.

In the second experiment, the same greenhouse gas forcing is used as in CO_2 only, but the effects of sulfate aerosols are added following the method described in Meehl et al. (1996). They concluded that twice the direct sulfate forcing was a representative approximation of the combined effects of sulfate aerosol direct and indirect forcing, with the magnitude of the forcing being most important. Therefore, for simplicity and given the great uncertainties surrounding sulfate aerosol forcing, the 2 × direct forcing from Meehl et al. (1996) was adopted. The time evolution of sulfate aerosol forcing for the period 1900–90 (starting from zero in 1900; though not actually zero at that time, the forcing was small and assumed to be zero for the purposes of these experiments) was scaled to follow the smoothed emission rates of Boden et al. (1994; Fig. 1b). In Fig. 1a the time evolution of the net radiative forcing (CO_2 + sulfates) shows small increases from 1900 to around 1940

from increasing CO_2 (less than 0.2 W m^{-2}). Then the net forcing decreases slightly (roughly 0.3 W m^{-2}) until the early 1960s as sulfate aerosol negative forcing makes a significant contribution. After that it increases rapidly from about 0.2 W m^{-2} to over 3 W m^{-2} in 2035 as the positive forcing from increasing CO_2 again makes the dominant contribution to the overall forcing.

The patterns of the 1990 forcing for CO_2 only, sulfates only, and CO_2 + sulfates are shown in Fig. 2 for the December–February (DJF) and June–August (JJA) seasons. As noted in earlier studies, CO_2 radiative forcing is globally positive for both seasons. Negative sulfate radiative forcing (meant to represent direct plus indirect effects, with caveats noted above concerning the simplicity of this formulation) is confined to regions in the vicinity where emissions are highest corresponding to areas of greatest industrial activity. It is larger in JJA (-1.78 W m^{-2} globally averaged), because of the sun being more directly overhead in the Northern Hemisphere, than in DJF (-0.82 W m^{-2} globally averaged). The 1990 global annually averaged total radiative forcing from sulfate aerosols accounting for direct and indirect effects is -1.30 W m^{-2} [-0.65 W m^{-2} for the direct effect, as compared with the estimated range of -0.2 W m^{-2} to -0.8 W m^{-2} from Houghton et al. (1996) and a recent estimate of -0.72 W m^{-2} over ocean areas by Haywood et al. (1999), and -0.65 W m^{-2} for the indirect effect, as compared with the estimated range of 0 to -1.5 W m^{-2} from Houghton et al. (1996)]. The net forcing for CO_2 + sulfates shows positive radiative forcing for 1990 (Fig. 2) almost everywhere outside of North America and Eurasia during DJF, while in JJA the negative forcing from sulfates dominates almost the entire Northern Hemisphere, with positive forcing in the Southern Hemisphere. The global annually averaged forcing from greenhouse gases for 1990 is +2.44 W m^{-2}, and when added to the negative radiative forcing from sulfate aerosols gives a net radiative forcing of +1.14 W m^{-2}.

After 1990, the forcing follows the regional time evolution of the IS92a scenario as depicted by Mitchell et al. (1995a), with biggest increases of sulfate aerosol forcing occurring over Asia. Figure 3 is similar to Fig. 2 and shows the radiative forcing for the year 2030. There is much similarity of the patterns between Fig. 2 and Fig. 3, except that Fig. 3 shows the effects of the increased negative forcing from the sulfates, as well as greater positive forcing from CO_2. Because, as shown in Fig. 1, the positive radiative forcing from CO_2 increases at a greater rate than the negative forcing from sulfates after 1990, the positive forcing dominates the negative forcing in more areas of the globe in Fig. 3, such that there are only small net negative forcing regions over North America during DJF, and more confined negative forcing areas during JJA over North America, the North Atlantic, and North Pacific. For sulfate aerosols (direct plus indirect effect), the total annual radiative forcing for 2030 is -1.82 W m^{-2} (-1.28 W m^{-2} for DJF, -2.38 W m^{-2} for JJA). Added to the annual mean greenhouse gas forcing of +4.8 W m^{-2}, the annual mean net radiative forcing for 2030 is +2.98 W m^{-2}.

Of course there are other forcing factors that contribute to the time evolution of the climate system (e.g., solar, soot, biomass burning, volcanos, etc.). There are also large uncertainties (discussed above) in the magnitude of the sulfate aerosol forcing. Thus the time evolution of the net radiative forcing in Fig. 1 has its own large uncertainties. However, for our purposes we require mainly a time-varying external forcing against which to evaluate changes in decadal variability. The details of the forcing could change but we are mostly interested in the associated large-scale changes of the mean climate base state and characteristics of decadal variability in the model.

3. Globally averaged climate change

Figure 4 shows the time evolution of the globally averaged surface air temperature for the CO_2-only and CO_2 + sulfates experiments compared to the control experiment and observations. As could be expected from the forcing in Fig. 1, the CO_2 + sulfates shows less overall warming than the CO_2-only experiment as has been seen in previous experiments. Though there is considerable decadal and longer timescale variability evident in the time series that obviously affects the average differences, similar problems exist in the observations. Thus it is useful to calculate some benchmark temperature change numbers for comparison between model and observations. For the annual mean 20-yr average 1981–2000, CO_2 only minus a long-term mean of the first 95 yr of the control run, the globally averaged surface air temperature difference is +1.6°C, and for CO_2 + sulfates minus control the value is +0.6°C. For the period 2016–35, CO_2 only minus control is +4.1°C, and CO_2 + sulfates minus control is +2.3°C.

For the period in the observations from 1981 to 1997, the globally averaged surface air temperature increase relative to the period 1900–19 is +0.6°C, which is comparable to the value of +0.6°C for the model experiment with CO_2 + sulfates calculated over the slightly longer period 1981–2000. For direct comparison, the globally averaged surface air temperature change from the coupled model for years 1981–97 is +0.5°C. For this time period and these forcings, the model response is at least not totally out of line with what has been observed, even though there are many more forcings at work in the observed system. Probably, as noted above, this correspondence is mainly fortuitous given the large uncertainties in magnitude of sulfate aerosol forcing and model sensitivity.

As could be expected from previous studies cited earlier, the time evolution of the globally averaged temperatures from both experiments roughly follows the corresponding radiative forcing in Fig. 1. The correlation of normalized 7-yr running mean [to remove ENSO

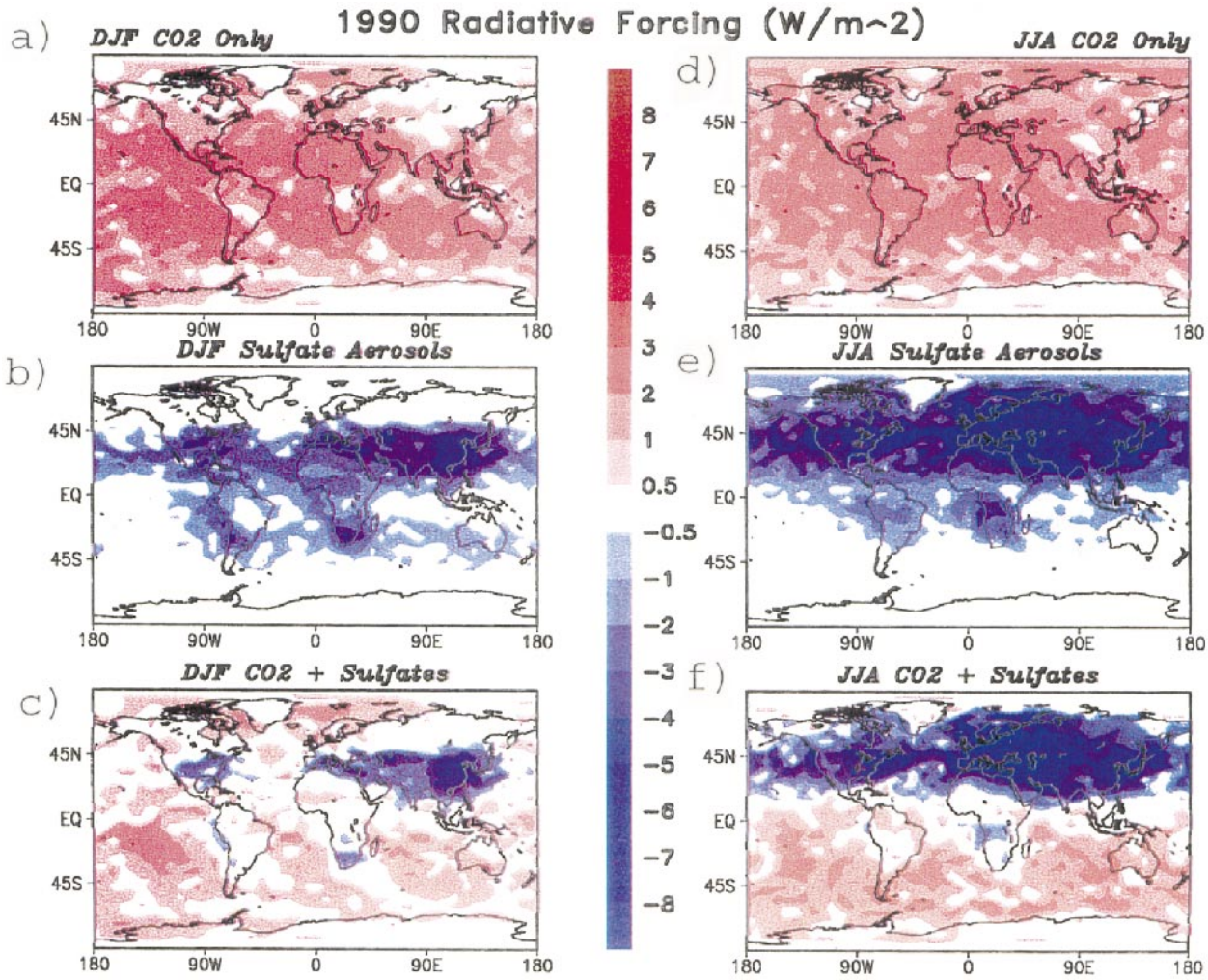

FIG. 2. (a) Radiative forcing (W m^{-2}) for 1990, CO_2 only, DJF; (b) same as (a) except for sulfate aerosols only; (c) same as (a) except for the net radiative forcing, CO_2 + sulfates; (d) same as (a) except for JJA; (e) same as (b) except for JJA; (f) same as (c) except for JJA.

variability following Kang (1996)] globally averaged surface air temperature from Fig. 4 with the normalized forcing from Fig. 1 is +0.77 for CO_2 only, and +0.63 for CO_2 + sulfates, both significant at greater than the 5% level.

To identify the main timescales of climate variability, we first look at detrended time series of globally averaged temperatures as a simple way of identifying relative timescales of variability [e.g., Lau and Weng (1999), identified a linear trend, decadal, and ENSO variability in post-World War II (WWII) observations]. Then we will filter the original raw nondetrended data to focus on a specific timescale.

Figure 5 shows spectra of detrended globally averaged surface air temperature for the period 1900–94 for the observations [Fig. 5a derived from the ''IPCC'' observed surface temperature dataset, e.g., Jones (1994)], the CO_2-only experiment from 1900 to 1994 (Fig. 5c), and the CO_2 + sulfates experiment from 1900 to 1994 (Fig. 5d), along with a spectra of 95 yr (the same number of years as the observations) of the control run (Fig. 5b). The spectra are calculated using the Fourier transform method with a 10% taper applied to the time series to avoid aliasing (Jenkins and Watts 1969). Note that the *y* axes are scaled differently between panels. Comparable spectra of the raw data (not shown) have similar spectral peaks but with accordingly larger amplitude power at the very lowest periods reflecting the warming trend in the data.

In comparing the observations with the control run, both spectra are red with low-frequency power above the red noise estimate (red noise spectra are computed based on the lag-one autocorrelation of the annual data) around 10 years for the observations (note that filtering out the very low frequency variability changes the red noise estimate and enhances the contribution from the power around 10 years, not shown) and 13.5 yr for the coupled model. Additionally, there are maxima in the

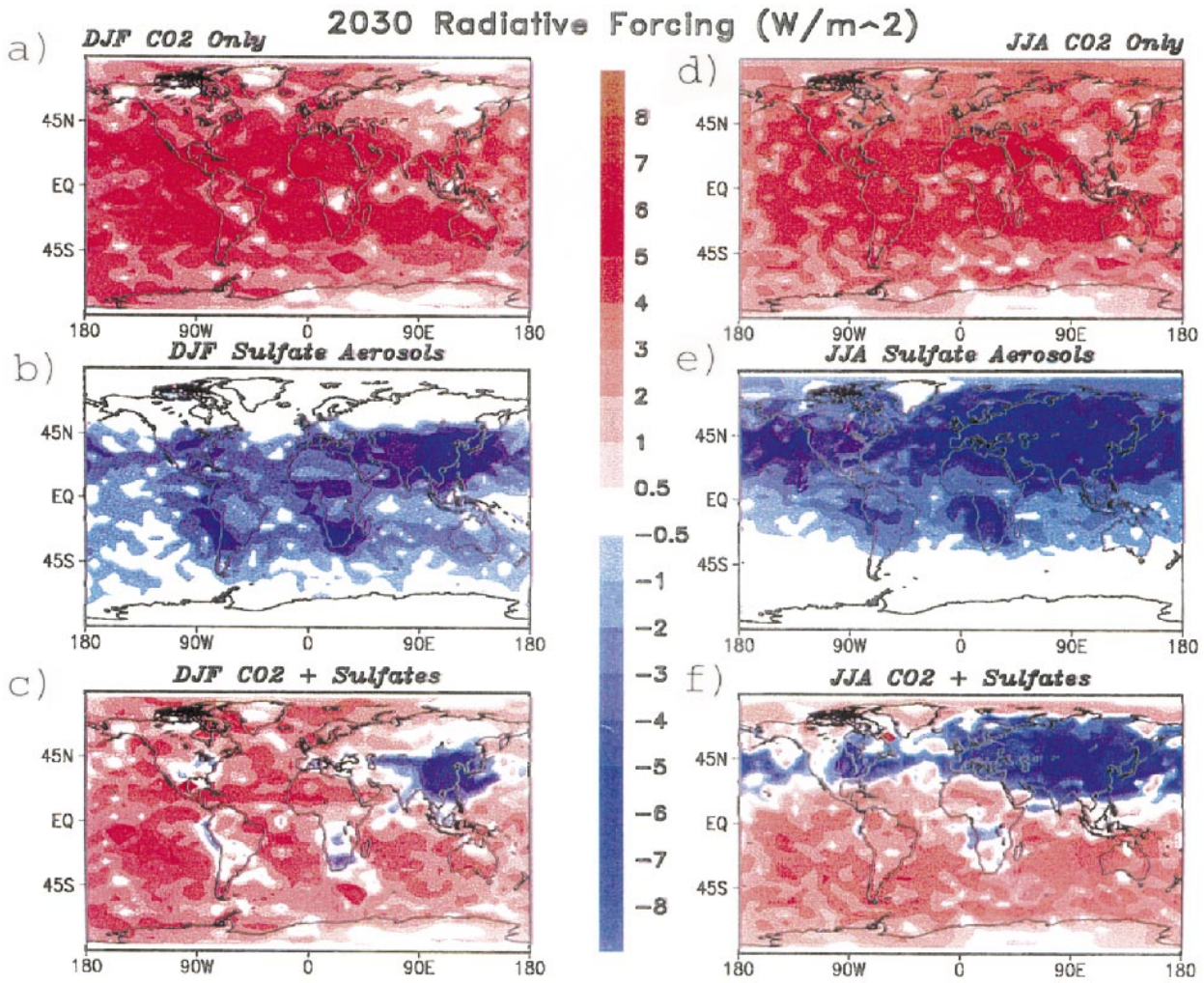

FIG. 3. Same as Fig. 2 but for the year 2030.

El Niño periods of around 3.5 and 6 yr in the observations, and 4 and 6 yr in the coupled model control integration. There may be some biases due to detrending technique or the unresolved low or high frequencies (Madden and Jones 1997). However, sensitivity tests with nondetrended data, high-frequency filtering, or different time sampling (e.g., monthly) show that effects of aliasing on the low frequencies (i.e., periods greater than 10 yr) are minimal.

An EOF analysis of low-pass filtered surface temperature for the coupled model shows an El Niño–like pattern [greater warming in the central and eastern tropical Pacific in comparison with the western Pacific; Meehl et al. (1998), Fig. 1a] with characteristics noted in observations (e.g., Zhang et al. 1997). For example, the low frequencies are characterized by a broader off-equatorial pattern of positive values in the tropical Pacific. The interannual timescale pattern from the high-pass filtered model data shows systematic errors characteristic of other global coupled models (e.g., Meehl and Arblaster 1998) with El Niño variability centered farther west than in observations (e.g., Zhang et al. 1997), and with weaker amplitude (Meehl et al. 1998, Fig. 1c).

A likely mechanism for the internally generated decadal timescale variability in this coupled model is described by Meehl et al. (1998, 2000a). Ocean heat content anomalies embedded in the gyre circulations of the Pacific, Atlantic, and Indian Oceans are associated with global decadal timescale El Niño–like signals in atmosphere and ocean with consequent global energy balance variations. Large-scale tropical–midlatitude interactions act to replenish the ocean heat content anomalies. Maxima in decadal timescale globally averaged surface temperature occur in conjunction with periodic arrangements of SST anomalies, in association with the heat content anomalies embedded in the various ocean gyre circulations, in a global El Niño–like pattern that is highly correlated with such maxima. Of particular relevance to results in this paper, the decadal timescale

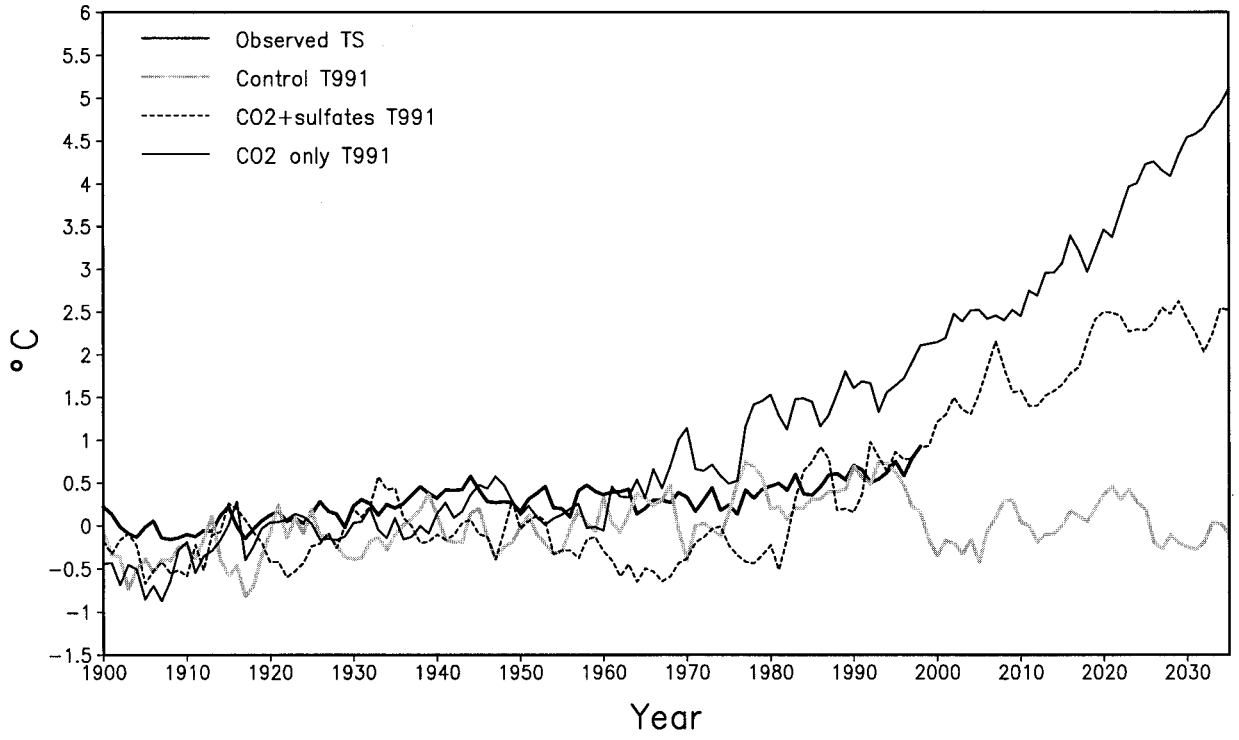

FIG. 4. 1-yr running-mean time series of globally averaged surface temperature anomalies for the control run, CO_2-only experiment minus control from 1900 to 2035, CO_2 + sulfates minus control from 1900–2035, and observations (Jones 1994), using 1890–1910 as base period.

in the model is approximately set by the climate base state related to the circuit times of the ocean gyre circulations. The somewhat longer decadal period for the model relates to simulated ocean gyre circulations that are weaker than observed (Meehl et al. 1998). Consequently, in a sensitivity experiment with this model in which a sea-ice parameter is changed, a weakening of the base-state surface wind stress and upper ocean currents results in a decrease of 10–20-yr period variability and increased lower-frequency variability (periods greater than 20 yr) of surface temperature (Meehl et al. 2000a).

In the observations in Fig. 5a there is enhanced power at periods greater than about 20 yr that is not evident in the coupled model control run in Fig. 5b. In the CO_2-only and CO_2 + sulfates experiments in Figs. 5c and 5d, there is also enhanced power at those low frequencies. Averaging the power at periods greater than 19 yr, forming an f ratio with a similar average from the control run, and estimating degrees of freedom as 2 times the number of frequencies in the averaging window (Blackman and Tukey 1958), the CO_2-only f ratio is 9.5 (significant at the 1% level for 8 degrees of freedom), and the CO_2 + sulfates is 14.0 (significant at the 1% level for 8 degrees of freedom; note that this is a ratio of variances—thus the application of the f statistic). Thus for globally averaged surface temperature, there is significantly enhanced power at periods longer than about 20 yr in the two anthropogenic climate change experiments as compared with the control run. This indicates the external forcing in the two climate change experiments has introduced low-frequency variability into the climate system at periods greater than 20 yr, consistent with previous studies. Meanwhile for the decadal (10–20 yr) periods, there is an apparent decrease of variability of globally averaged temperature in both the climate change experiments. The f ratio for CO_2 + sulfates is 1.6 (not a significant decrease), and the f ratio for the decrease of variability in the CO_2-only experiment is 2.1, not quite significant at the 10% level of 2.3 for 10 degrees of freedom. Thus, changes in globally averaged surface temperature indicate significantly enhanced power at periods greater than about 20 yr, and marginal decreases of power for 10–20-yr periods.

Having now identified candidate variability changes at various timescales, in section 5 we will filter the original nondetrended data to look at the patterns and associated changes of variability on the 10–20-yr timescale. Next we look at mean climate change patterns to document changes in the base state due to changes in radiative forcing in the model.

4. Patterns of climate change

Twenty-year averages are calculated to provide a representation of change in the climate base state in the model in the first part of the twenty-first century (2016–

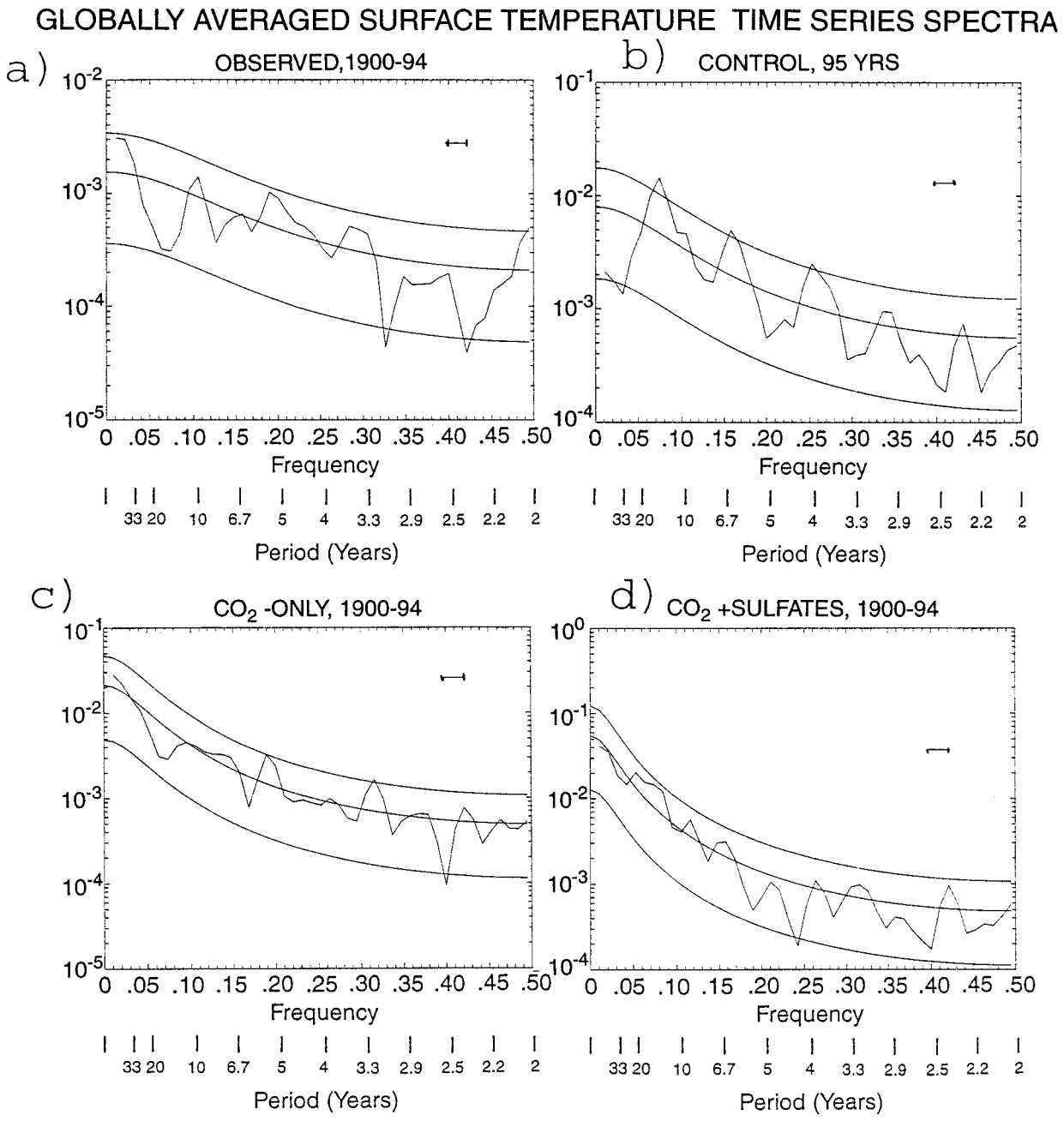

FIG. 5. Power spectra of global annually averaged surface temperature time series for (a) observations from 1900 to 1994; (b) coupled model control run, 95 yr; (c) CO_2-only coupled model experiment from 1900 to 1994; (d) CO_2 + sulfates coupled model experiment from 1900 to 1994. Superimposed smooth lines are red noise (middle), and 5% and 95% confidence limits. Bandwidth is shown in upper-right-hand part of each panel. Note that the *y* axes are scaled differently between the panels.

35). The mean control climate is taken as an average over the first 95 yr. Differences for the CO_2-only experiment [the 1% yr^{-1} CO_2 increase sensitivity experiment by Meehl et al. (1996)] are not shown here since the patterns are similar to the CO_2 + sulfates results but with larger overall warming as indicated by the global averages shown earlier. Results from the CO_2-only experiment will be included later in the EOF analysis. Because of the aspects of decadal variability discussed below, the fact that these are single realizations, and given the large uncertainties in the sulfate forcing, values for any particular averaging period would vary in detailed significance tests. Therefore, standard deviations are referred to for guidance to put the broad-scale climate change differences in context in relation to model variability.

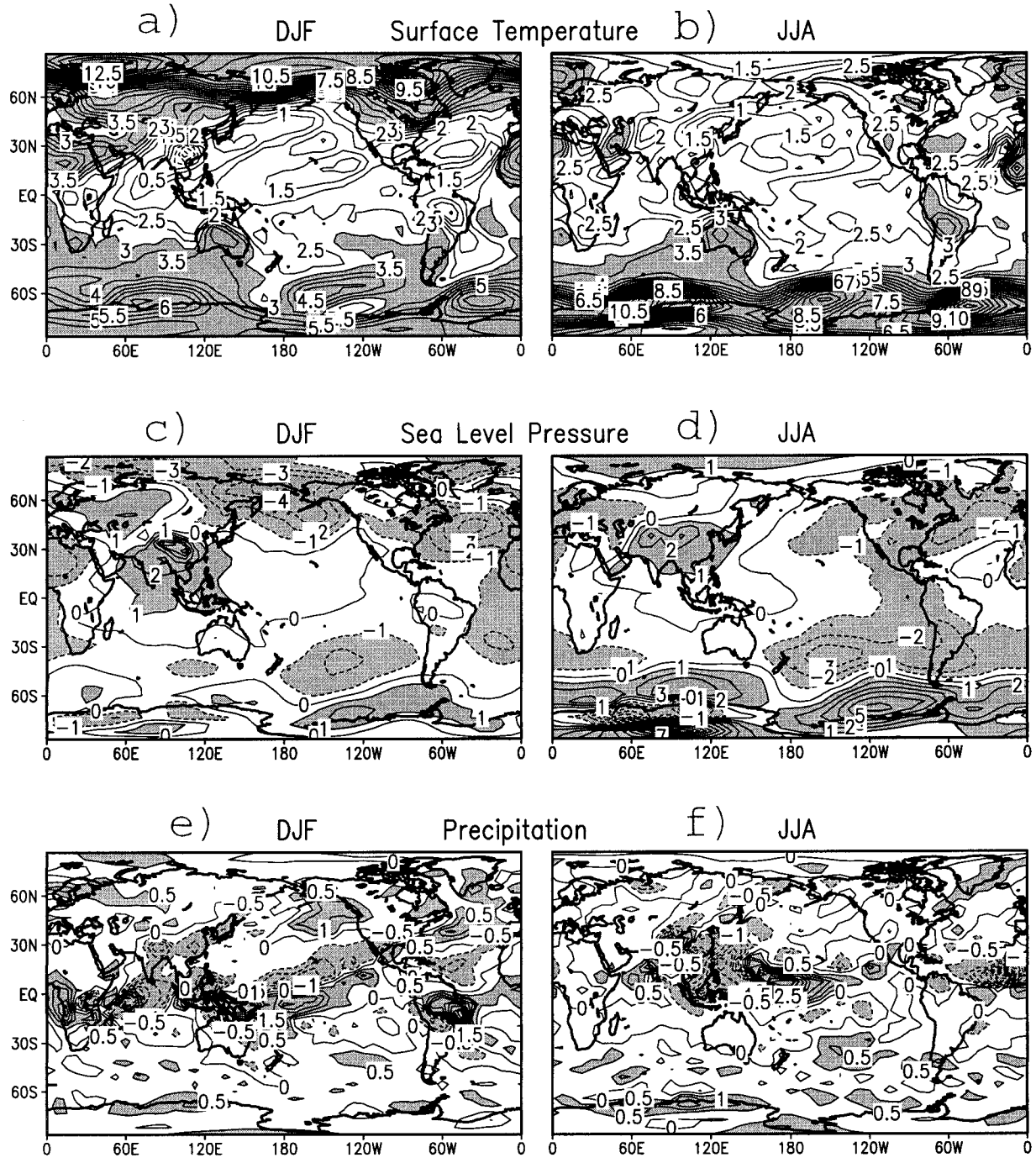

FIG. 6. (a) For the DJF season, time-averaged differences for surface air temperature (temperature of the lowest model layer at sigma level 0.991), 2016–35, CO_2 + sulfates minus long-term mean (95 yr) control; (b) same as (a) except for JJA; (c) same as (a) except for sea level pressure (mb); (d) same as (c) except for JJA; (e) same as (a) except for precipitation (mm day^{-1}); (f) same as (e) except for JJA. Contour interval is 0.5°C for temperature and 1 mb for SLP. Shading indicates differences greater than 3.0°C for temperature or ±1.0 mb for SLP, and ±0.5 mm day^{-1} for precipitation.

For the model there is warming greater than one standard deviation almost everywhere (Figs. 6a,b), but with relatively smaller amplitude warming (less than +2°C) in the sulfate aerosol regions. Thus, though the warming response from increasing CO_2 overwhelms the cooling from sulfate aerosols, the influence of the sulfate aerosols is still evident in the regional patterns of warming. Temperature standard deviations in these regions are about 1°–2°C.

Another persistent feature in the warming pattern for

both seasons in Fig. 6 is the El Niño–like response in the tropical Pacific discussed earlier (e.g., Meehl and Washington 1996; Knutson and Manabe 1998; Timmermann et al. 1999). That is, there is greater warming (nearly a degree for DJF, and more than 1.5°C for JJA) in the central and eastern equatorial Pacific as compared with the western equatorial Pacific. One standard deviation in these regions is about 0.5°C–1.0°C in the eastern equatorial Pacific in the model, and less than 0.5°C in the western equatorial Pacific.

The El Niño–like pattern is evident in the SLP differences in Fig. 6 for the model as well. For both seasons, as in the surface temperature differences, there is evidence of this pattern characterized by negative SLP differences of around 0.5 mb or less over the tropical eastern Pacific during DJF, and positive SLP differences of 1.0 mb or more over the south Asian and Indian Ocean regions. (One standard deviation in these regions is about 0.5–1.0 mb.) In the areas of the midlatitude North and South Pacific troughs there are negative SLP differences of −1.5 mb or larger amplitude (though southward shifted in the North Pacific in JJA), with the greatest magnitude negative SLP differences of 2 mb and larger occurring in the winter hemisphere for the 1981–2000 period. (One standard deviation in these regions is about 3 mb in the winter hemisphere.) There are negative SLP anomalies in the tropical and subtropical Atlantic during DJF in the model in Fig. 6c, with negative SLP anomalies in the North Atlantic in DJF and JJA (Figs. 6c,d).

The precipitation differences associated with these patterns of climate change from surface temperature and SLP are shown in Figs. 6e,f. As could be expected from the El Niño–like patterns in Figs. 6a,b and the results shown for the increased CO_2 sensitivity experiment (Meehl and Washington 1996), there is a comparable precipitation anomaly pattern for both seasons with enhanced precipitation near the date line in the central equatorial Pacific greater than roughly +3 mm day^{-1} (increases of 30% and more), with mostly comparable decreases over the far western Pacific, Indian Ocean, and south Asia. [Note that the pattern and magnitude of climatological mean precipitation are well represented in the coupled model as shown by Meehl and Washington (1995, Fig. 3b).] Interannual standard deviations of precipitation in these regions in Fig. 6 are roughly 1–3 mm day^{-1}.

Consistent with the results from the sensitivity experiments of Meehl et al. (1996), JJA south Asian monsoon precipitation (defined as precipitation averaged over land points in the area 5°–40°N, 60°–100°E) decreases in the CO_2 + sulfates experiment by 6.2% for future climate (2016–35). There is inherent decadal variability of Indian monsoon rainfall as represented by an all-India precipitation index for the observations (Parthasarathy et al. 1991) and in the coupled model control run (Meehl et al. 1998). With the addition of the negative radiative forcing from sulfates (e.g., Fig. 2), the south Asian landmass warms more slowly than the ocean, decreasing land–sea temperature contrast [as shown to have occurred in the post-WWII surface temperature observations; Meehl and Washington (1993)] and weakening the Indian monsoon here by 6.2% as in some other model simulations (Lal et al. 1995; Meehl et al. 1996; Mitchell and Johns 1997; Boucher et al. 1998). However, these results are clearly dependent on the scenario used for future sulfate aerosol concentrations over south Asia and the averaging period since recent scenarios for sulfate aerosols over south Asia for the end of the twenty-first century show decreases (from mid–twenty-first-century high levels) almost back to present-day levels (Dai et al. 2000).

The Australian monsoon in DJF (defined as precipitation averaged over the area 5°N–25°S, 100°–145°E) is little changed (+0.2%) in future climate in this model for the period 2016–35. Additionally, there are indications of decreased rainfall (differences about −2.0 mm day^{-1} or decreases of roughly 20%) during the JJA season in the Sahel region of Africa in the model (Fig. 6f).

5. Decadal variability and climate change

Attempts to estimate the natural unforced low-frequency variability are complicated by the fact that it is difficult to remove the effects of the forcing a priori from the observed data. There are a number of ways that have been proposed to do this in terms of optimal fingerprints and others (e.g., Hegerl et al. 1997). Here we are not performing a climate change detection/attribution study, but we are interested in patterns of decadal timescale variability and how changes in that variability could occur in a climate with a changed base state and low-frequency forcing (periods greater than 20 yr) superimposed.

To illustrate this spatially, the pattern of the first EOF from a 95-yr period of the control run in Fig. 7a can be compared with the first EOF from the nondetrended twentieth-century experiment (1900–94) for CO_2 + sulfates in Fig. 8a. A similar El Niño–like pattern to that seen in the control run, CO_2 only, and the observations (e.g., Lau and Weng 1999) is evident [pattern correlation with the control in Fig. 7a is +0.86, and +0.82 with CO_2 only (not shown, but with a very similar pattern)]. The El Niño–like pattern is characterized by large positive values greater than +0.6 in the central and eastern equatorial Pacific, and opposite sign values in the northwest and southwest Pacific.

In comparing the EOF1 principal component (PC) time series in Fig. 8b to a similar plot from the control in Fig. 7b, there is evidence of decadal variability but also low-frequency variability with a comparable time evolution to the forcing (superimposed in Fig. 8b from Fig. 1a). If the EOF calculation includes the future climate period (Fig. 8c), the pattern still has similarities to that for the twentieth century in Fig. 8a, but the

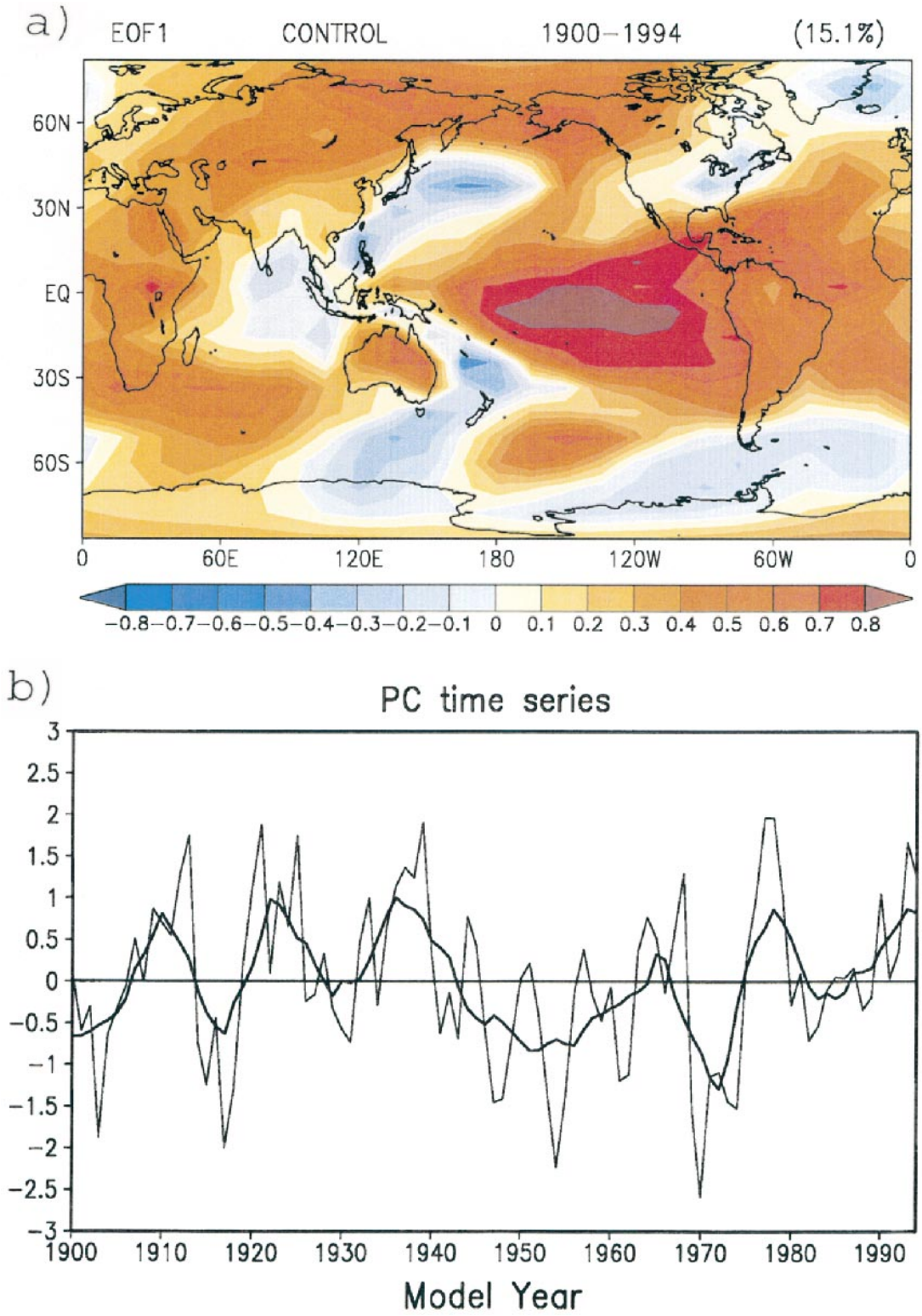

FIG. 7. (a) EOF1 for annual mean surface temperature for 95 yr from the coupled model control integration, explained variance in parentheses; (b) normalized principle component time series of EOF1 in part (a), with 7-yr running mean superimposed on the annual mean time series.

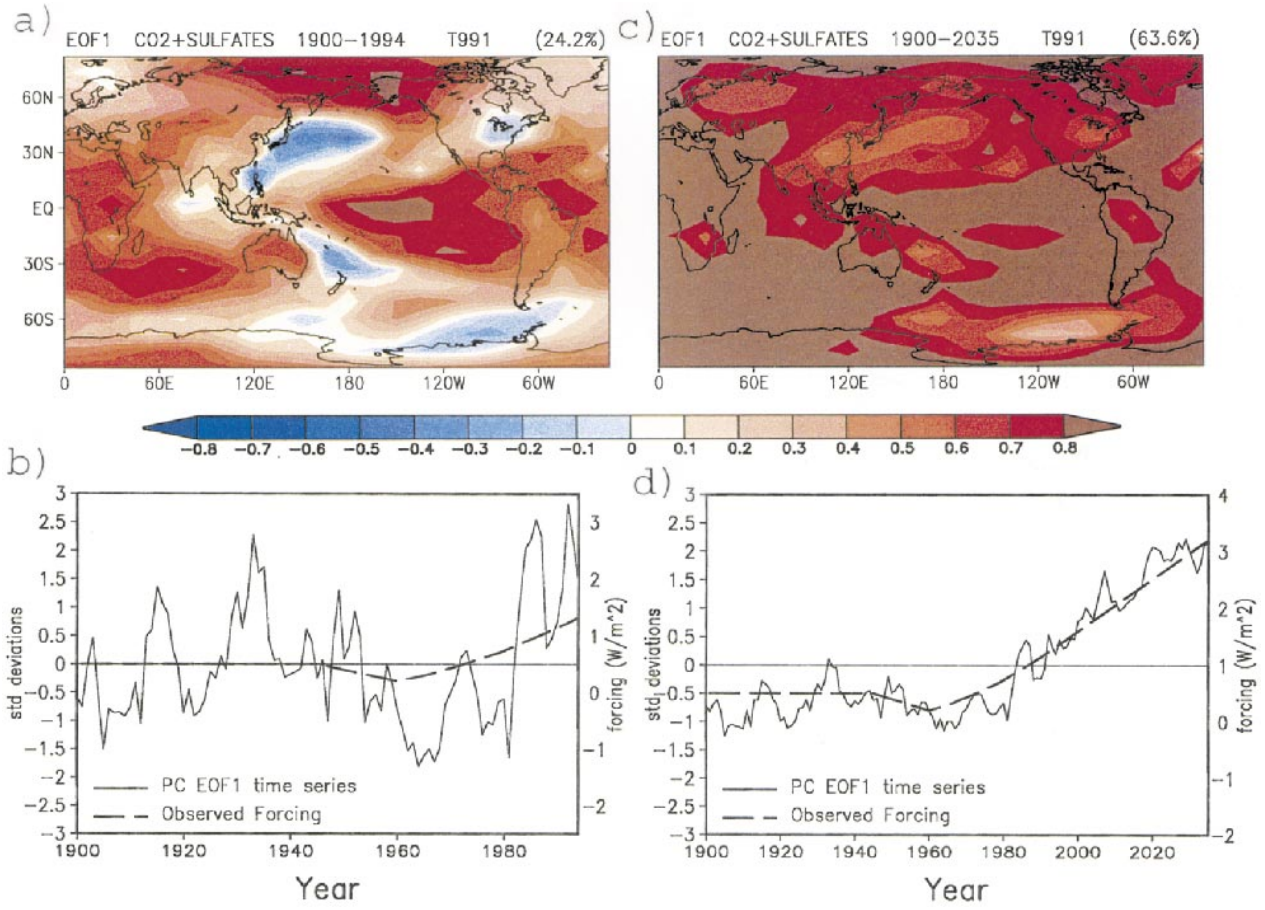

FIG. 8. (a) EOF1 for annual mean surface temperature from CO_2 + sulfates experiment, 1900–94, explained variance in parentheses; (b) normalized principle component time series of EOF1 in (a), with forcing from Fig. 1a superimposed as dashed line (scale for PC time series at left, forcing scale at right); (c) EOF1 for annual mean surface temperature from CO_2 + sulfates experiment, 1900–2035, explained variance in parentheses; (b) normalized principle component time series of EOF1 in (c), with forcing from Fig. 1a superimposed as dashed line (scale for PC time series at left, forcing scale at right).

overwhelming effects of the warming from increasing greenhouse gases is evidenced by values of nearly all positive sign in Fig. 8c, and a PC time series in Fig. 8d that again reflects the forcing (superimposed in Fig. 8d from Fig. 1a) as the climate system warms significantly by 2035.

The question, then, is what effect, if any, does this time-varying external forcing and significant change in base state from that forcing have on the decadal (10–20-yr period) variability? To address this question, we first filter the raw nondetrended observed and model monthly anomaly data with a Lanczos digital bandpass filter with cutoffs at 10 and 20 yr to isolate variability on that timescale. Using 433 weights results in a shorter time series running from 1919 to 2017 in the model, and from 1918 to 1976 in the observations. A second calculation was performed using 217 weights, and results were very similar. Therefore, for the observations the latter is used to allow a somewhat longer time series to be included (from 1912 to 1985, tick marks on PC time series correspond to 1 January of each year). We also calculate the spectra of the filtered data using just the last half of the model time series (after 1968) when the forcing is changing most dramatically (Fig. 1a), to emphasize possible changes that could result in the decadal timescale variability during that period. There is no detrending of the data either before or after filtering.

Figure 9 shows the first EOF of the filtered data from observations [Global Sea-Ice and Sea Surface Temperature Data Set (GISST) original time series runs from 1903 to 1994; Parker et al. (1995); Rayner et al. (1996)] and the model control run (135 yr). The GISST dataset is used here because the data gaps have been filled to provide a continuous time series at all ocean points. The familiar El Niño–like pattern (as defined above, with large positive values in the tropical central and western Pacific, and opposite sign values in the North and South Pacific) is evident as could be expected from previous analyses (Figs. 7 and 8). Though the GISST data cover ocean areas only and the model data are global, certain similarities, such as the pattern in the Pacific, are evident (noted earlier in Fig. 7). Main areas of disagreement

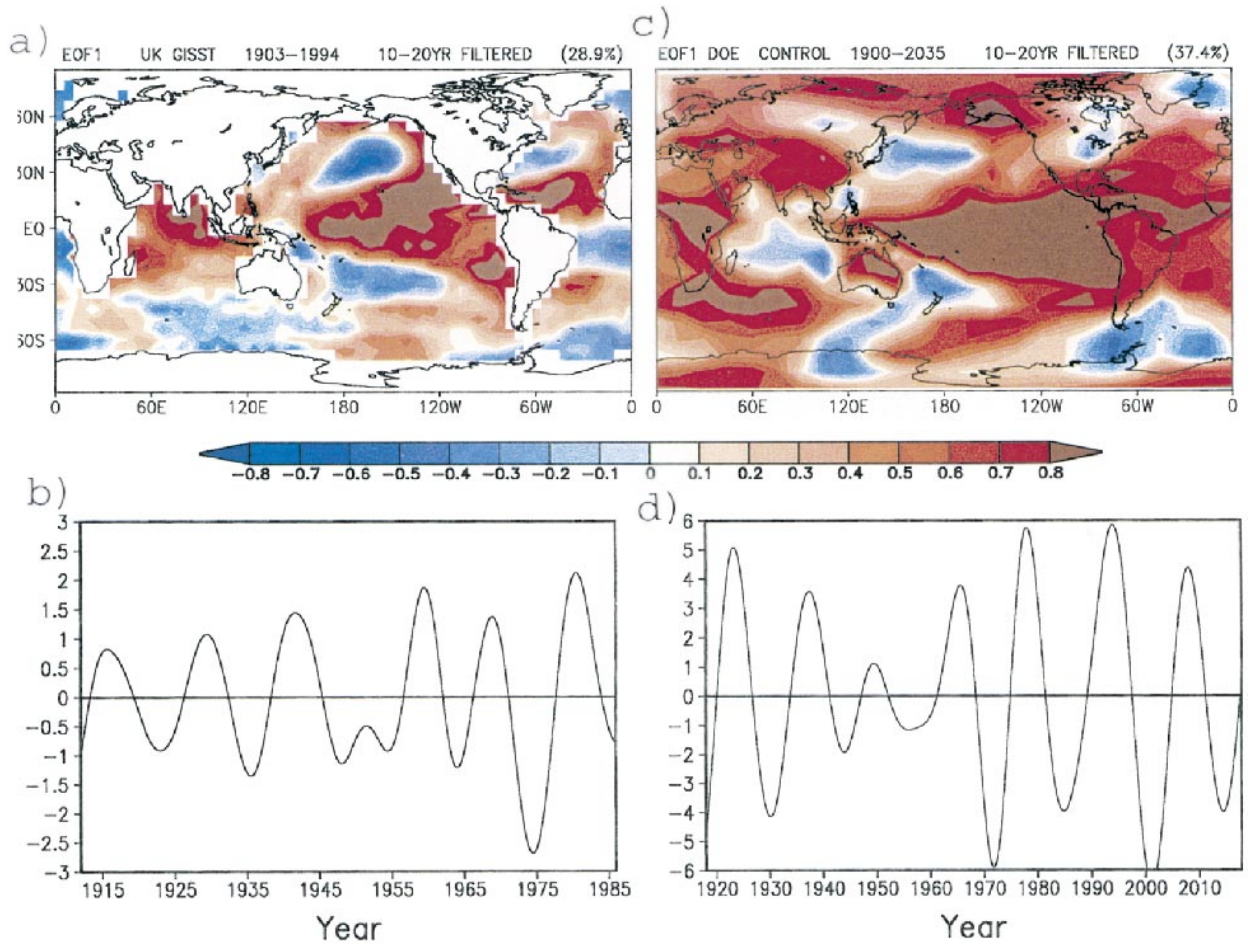

FIG. 9. (a) EOF1 for bandpass filtered decadal (10–20 yr) annual mean surface temperature from GISST observations (Parker et al. 1995; Rayner et al. 1996), 1903–94 (truncated from 1912 to 1985 after filtering), explained variance in parentheses; (b) nonnormalized principal component time series of EOF1 in (a); (c) EOF1 for bandpass filtered decadal (10–20 yr) annual mean surface temperature from model control run, 1900–2035 (truncated from 1919 to 2017 after filtering), explained variance in parentheses; (d) nonnormalized principal component time series of EOF1 in (c).

between the two are in the eastern Indian Ocean and tropical Atlantic. The former has to do with the anomalous westward extent of the eastern Pacific cold tongue regime mentioned above. This moves the Walker circulation westward, and affects the eastern Indian Ocean as a consequence. As could have been anticipated from Fig. 5, the amplitude of the nonnormalized PC time series from the model (Fig. 9d) is over twice the observed (Fig. 9b), illustrating again the strong decadal variability in this model.

Comparable filtering is done for the CO_2 + sulfates and CO_2−only experiments, and the resulting EOFs are shown in Fig. 10. Both have similar patterns to the control run (pattern correlations of +0.68 and +0.67, respectively). The pattern in Fig. 10c for CO_2 only has reduced magnitude in comparison with the control and CO_2 + sulfates, and there are lower amplitude values of the PC time series in Fig. 10d in comparison with the control in Fig. 9c and CO_2 + sulfates in Fig. 10b. Spectra are then calculated from the respective PC time series and shown in Fig. 11a. It is apparent that the power in the 10–20-yr band has decreased somewhat from the control in CO_2 + sulfates, but is appreciably smaller in CO_2−only (seen also for spectra of the original EOF PC time series of the raw data in Figs. 7 and 8; not shown). If the values are averaged over the window of the filtering in Fig. 12a (10–20 yr), the resulting f test performed as described earlier shows an f value of 1.19 for CO_2 + SO_4 in comparison with the control, and 2.37 for CO_2 only. For the 6 frequencies and consequent 12 degrees of freedom, the decrease of power in the 10–20-yr window is not significant for CO_2 + sulfates, but is significant at the 10% level for CO_2 only. A similar calculation using only the second half of the time series described above is shown in Fig. 11b. Though the shorter time series presents a serious limitation for this calculation, the CO_2 only still shows a significant decrease in the amplitude of decadal variability (using frequencies approximating the 10–20-yr period window bracketing 10–25-yr periods and 8 de-

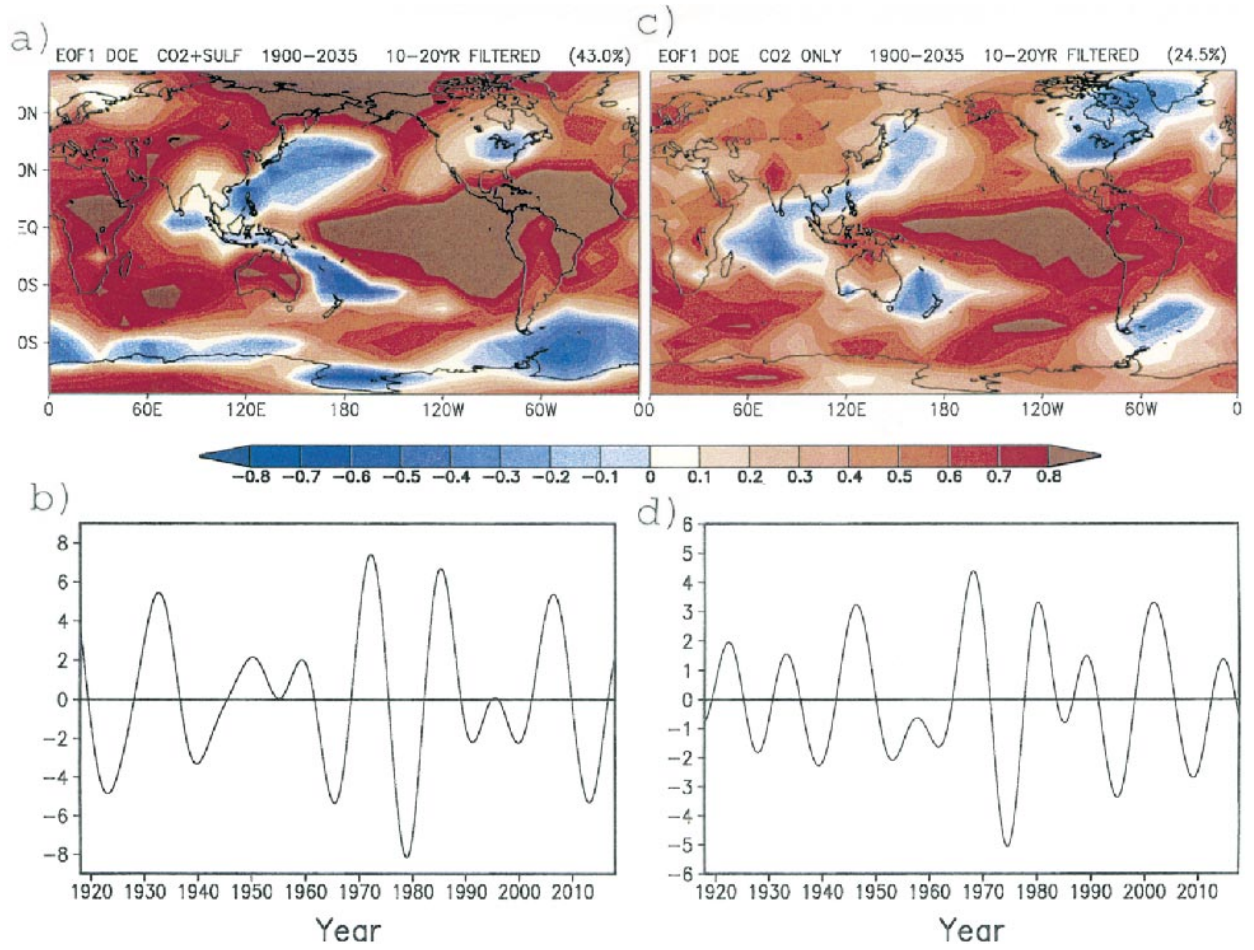

FIG. 10. (a) EOF1 for bandpass filtered decadal (10–20 yr) annual mean surface temperature from CO_2 + sulfates experiment, 1900–2035 (truncated from 1919 to 2017 after filtering), explained variance in parentheses; (b) nonnormalized principle component time series of EOF1 in (a); (c) EOF1 for bandpass filtered decadal (10–20 yr) annual mean surface temperature from CO_2−only experiment, 1900–2035 (truncated from 1919 to 2017 after filtering), explained variance in parentheses; (d) nonnormalized principle component time series of EOF1 in (c).

grees of freedom, the f value for CO_2 only in comparison with control is 3.05, which is significant at the 10% level).

Thus, with increasing positive forcing going from CO_2 + sulfates to CO_2 only, the pattern of the decadal variability is comparable but the magnitude reduced in these single-realization sensitivity experiments. We propose, based on the mechanism for decadal variability in this model described by Meehl et al. (1998, 2000a), the slackened equator-to-pole surface temperature gradient (Figs. 6a,b) with increasing CO_2 would be associated with a decrease of surface winds (implied in Figs. 6c,d) and the ocean gyre circulations would weaken concurrent with a reduction of the meridional overturning in the Atlantic. Indeed in Fig. 12 the magnitude of u component surface wind stress (averaged over the last 20 yr of the experiments) decreases in nearly all the ocean basins. Climatological westerlies and easterlies (Fig. 12a) both weaken (Fig. 12b), as signified by negative anomalies in westerly wind and upper ocean current regimes in the midlatitudes, and positive anomalies in easterly wind and current regimes in the tropics–subtropics. These changes range from about 5% to 20%, with some differences larger than 30% in the 20°–30°N Atlantic wind stress and 20°–40°S Pacific currents and wind stress. Though the ocean gyre circulations all consistently weaken, there are two exceptions in the wind stress, in the 20°–35°S Atlantic band, and the 35°–50°N Pacific band. The latter is influenced by the anomalous deepening of the Aleutian low (Fig. 6c) that overcomes the general decrease of equator-to-pole surface temperature gradient in that region due to remote forcing from the Tropics associated with the El Niño–like SST and precipitation response (Fig. 6e).

Additionally, the weakening of the overturning in the Atlantic also acts to slow down the ocean circulation. Maximum values of meridional overturning streamfunction in the Atlantic averaged over the last 20 yr of the CO_2-only experiment decrease roughly 50% compared to the control. This contributes to the reduced

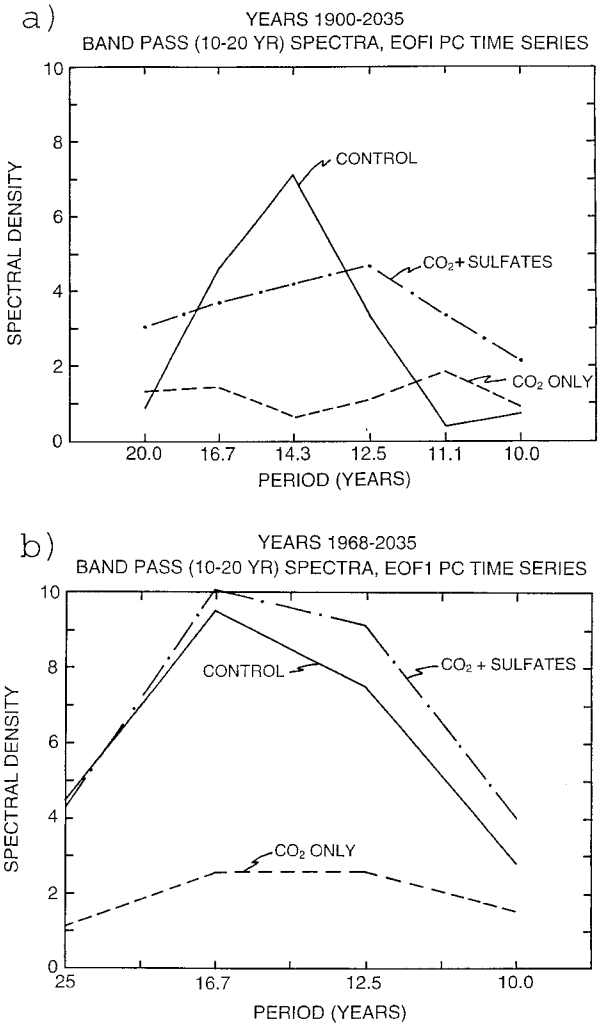

FIG. 11. (a) Spectra of EOF1 PC time series calculated from band-pass filtered decadal (10–20 yr) annual mean surface temperature, 1900–2035 (truncated from 1919 to 2017 after filtering), for model control run (solid line, PC time series in Fig. 13d), CO_2 + sulfates (dash–dot line, PC time series in Fig. 14b), and CO_2 only (dashed line, PC time series in Fig. 14d); (b) same as (a) except spectra calculated for second half of PC time series (post-1968).

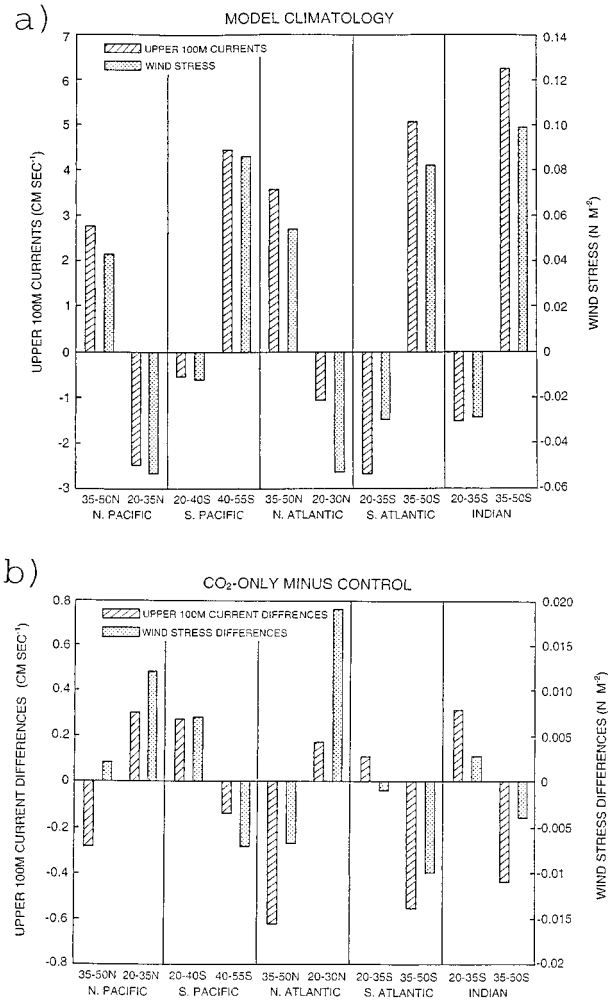

FIG. 12. (a) Upper-ocean (averaged over upper 100 m) *u*-component currents (cm sec^{-1}) and *u*-component wind stress (N m^{-2}), 76-yr averages from model control run, ocean basins, and latitude bands as indicated, North Atlantic longitude range is 70°–10°W, South Atlantic 60°W–20°E, North Pacific 130°E–130°W, South Pacific 150°E–80°W, and Indian 50°–130°E; (b) same as (a) except for CO_2 only (years 2026–35) minus control.

amplitude of decadal variability as also noted by Meehl et al. (2000a). Both of these processes would have the effect of increasing the period of low-frequency variability, with a reduction of power in the 10–20-yr decadal window. This decrease in the amplitude of decadal climate variability is only significant with large positive radiative forcing (+4.80 W m^{-2} in 2030 for CO_2 only in comparison with +2.98 W m^{-2} in CO_2 + sulfates) and consequently greater changes to the base state in the CO_2-only experiment.

6. Conclusions

Mean climate base-state changes and changes in decadal variability (10–20-yr period) are examined in sensitivity experiments of twentieth- and twenty-first-century climate with CO_2 increases only and CO_2 + sulfates. Surface albedo changes are used to account for the negative radiative forcing by doubling the direct effect that is noted to represent roughly the magnitude and pattern of direct and indirect sulfate aerosol forcing in a previous study (Meehl et al. 1996). This is recognized as a simplified approximation, but given the uncertainties with representing the direct and indirect effects of sulfate aerosols, this technique allows an accounting of the first-order effects such that the regional characteristics of the negative forcing are represented.

Two climate change experiments are performed, both starting in the year 1900. The first uses greenhouse gas radiative forcing (represented by equivalent CO_2) observed during the twentieth century, and extends green-

house gas forcing to the year 2035 by increasing CO_2 1% yr^{-1} compound after 1990 (CO_2-only experiment). The second includes the same greenhouse gas (equivalent CO_2) forcing as the first, but adds the effects of time-varying geographic distributions of monthly sulfate aerosol radiative forcing. The climate change experiments are compared with a 135-yr control experiment with no change in external forcing.

Climate system responses in the CO_2-only and CO_2 + sulfates experiments in this particular model are marked by greater warming at high latitudes in the winter hemisphere with a consequent slackening of the equator-to-pole surface temperature gradient, a decrease in surface westerlies in most regions, and weakening of the ocean gyre circulations. Additionally, an El Niño–like pattern is evident in surface temperature (greater SST warming in the eastern Pacific in comparison with the far west), precipitation (an eastward shift in precipitation in the tropical Pacific), and sea level pressure (lower pressure over the eastern tropical Pacific, deeper midlatitude troughs in the North and South Pacific, higher pressure over Australasia). There are decreases of the south Asian monsoon, though this is noted to be highly dependent on the time frame of the averaging period and the future sulfate aerosol scenario used over Asia.

Spectral analysis of globally averaged surface temperature and an EOF analysis of annual mean surface temperature indicates that low-frequency variability with periods greater than 20 yr is introduced into the model coupled climate system with the El Niño–like pattern associated with low-frequency timescales similar to the forcing as seen in previous studies. The surface temperature time series are filtered to retain only variability on the decadal timescale (10–20-yr periods) to examine the possible effects of this introduced low-frequency variability and changes of base state. The El Niño–like pattern of decadal variability seen in observations is evident in each of the filtered model time series (control, CO_2−only and CO_2 + sulfates), but the magnitude decreases with increasing positive forcing. Previous analyses of decadal variability in this global coupled model indicate such a change is likely due to the altered climate base state involved with a weakening of the surface winds and ocean gyre circulations with increased positive radiative forcing, together with a less intense meridional overturning in the North Atlantic. As a consequence, the amplitude of the decadal (10–20 yr) variability in the model is reduced. This change is only significant in the CO_2-only experiment with greater positive radiative forcing changes and larger changes to the climate base state. Meanwhile, the amplitude of climate variability at timescales greater than 20 yr increases in part from low-frequency variability in the forcing.

These results have two interesting implications that must be tested in other models. First, superimposing a pattern of low-frequency forcing with periods greater than 20 yr increases the amplitude of climate variability on those timescales, while changes to the base state due to increases of that radiative forcing reduce the amplitude of decadal (10–20-yr period) variability. Second, such changes of global decadal variability require a considerable increase in radiative forcing and consequently large changes in the climate base state to be significant in this model. Though these single realizations are analyzed as sensitivity experiments and consequently must be treated as such, a similar analysis methodology could be applied to multiple scenario experiments or ensemble integrations.

Acknowledgments. We acknowledge helpful discussions and consultations with Dennis Shea, Tim Hoar, John Weatherly, Roland Madden, Tom Wigley, Kevin Trenberth, James Hurrell, and Barbara Bailey. A portion of this study was supported by the Office of Biological and Environmental Research, U.S. Department of Energy, as part of its Climate Change Prediction Program.

REFERENCES

Blackman, R. B., and J. W. Tukey, 1958: *The Measurement of Power Spectra.* Dover Publication, 190 pp.

Boden, T. A., D. P. Kaiser, R. J. Sepanski, and F. W. Stoss, Eds., 1994: Trends 93. A Compendium of Data on Global Change. Oak Ridge National Laboratory, ORNL/CDIAC-65, Oak Ridge, TN, 983 pp. [Available from ORNL, Oak Ridge, TN 37831.]

Boucher, O., M. Pham, and R. Sadourny, 1998: General circulation model simulations of the Indian summer monsoon with increasing levels of sulphate aerosols. *Ann. Geophys.,* **16,** 346–352.

Capotondi, A., and W. R. Holland, 1999: Thermohaline circulation variability in the NCAR Climate System Model (CSM). NCAR Tech. Note TN-445 + STR, 45 pp. [Available from National Center for Atmospheric Research, P.O. Box 3000, Boulder, CO 80307.]

Collins, M., 2000: The El Niño–Southern Oscillation in the second Hadley Centre coupled model and its response to greenhouse warming. *J. Climate,* **13,** 1299–1312.

Dai, A., T. M. L. Wigley, B. A. Boville, J. T. Kiehl, and L. E. Buja, 2000: Climates of the twentieth and twenty-first centuries simulated by the NCAR Climate System Model. *J. Climate,* in press.

Hasselmann, K., and Coauthors, 1995: Detection of anthropogenic climate change using a fingerprint method. MPI Rep. 168, 24 pp. [Available from Max-Planck-Institut für Meteorologie, Bundesstrasse 55, 20147 Hamburg, Germany.]

Haywood, J. M., R. J. Stouffer, R. T. Wetherald, S. Manabe, and V. Ramaswamy, 1997: Transient response of a coupled model to estimated changes in greenhouse gas and sulfate concentrations. *Geophys. Res. Lett.,* **24,** 1335–1338.

——, V. Ramaswamy, and B. J. Soden, 1999: Tropospheric aerosol climate forcing in clear-sky satellite observations over the oceans. *Science,* **283,** 1299–1303.

Hegerl, G. C., K. Hasselmann, U. Cubasch, J. F. B. Mitchell, E. Roeckner, R. Voss, and J. Waszkewitz, 1997: Multi-fingerprint detection and attribution analysis of greenhouse gas, greenhouse gas-plus-aerosol and solar forced climate change. *Climate Dyn.,* **13,** 613–634.

Houghton, J. T., L. G. Meira Filho, B. A. Callander, N. Harris, A. Kattenberg, and K. Maskell, Eds., 1996: *Climate Change 1995: The Science of Climate Change.* Cambridge University Press, 527 pp.

Jenkins, G. M., and D. G. Watts, 1969: *Spectral Analysis and Its Applications.* Holden-Day, 525 pp.

Jones, P. D., 1994: Hemispheric surface air temperature variations: A reanalysis and an update to 1993. *J. Climate,* **7,** 1794–1802.

Kang, I.-S., 1996: Association of interannual and interdecadal vari-

ations of global-mean temperature with tropical Pacific SST appearing in a model and observations. *J. Climate,* **9,** 455–464.

Kattenberg, A., and Coauthors, 1996: Climate models—projections of future climate. *Climate Change 1995: The Science of Climate Change: Contribution of Working Group I to the Second Assessment Report of the Intergovernmental Panel on Climatic Change,* J. T. Houghton et al., Eds., Cambridge University Press, 285–357.

Knutson, T., and S. Manabe, 1995: Time-mean response over the tropical Pacific to increased CO_2 in a coupled ocean–atmosphere model. *J. Climate,* **8,** 2181–2199.

——, and ——, 1998: Model assessment of decadal variability and trends in the tropical Pacific Ocean. *J. Climate,* **11,** 2273–2296.

——, ——, and D. Gu, 1997: Simulated ENSO in a global coupled ocean–atmosphere model: Multidecadal amplitude modulation and CO_2 sensitivity. *J. Climate,* **10,** 138–161.

Lal, M., U. Cubasch, R. Voss, and J. Waszkewitz, 1995: Effect of transient increase in greenhouse gases and sulphate aerosols on monsoon climate. *Curr. Sci.,* **69,** 752–763.

Lau, K.-M., and H. Weng, 1999: Interannual, decadal–interdecadal and global warming signals in sea surface temperature during 1955–97. *J. Climate,* **12,** 1257–1267.

Levitus, S., 1982: *Climatological Atlas of the World Ocean.* NOAA Professional Paper 13, 173 pp.

Madden, R. A., and R. H. Jones, 1997: The effect of likely biases in estimating the variance of long time averages of climatological data. *J. Climate,* **10,** 268–272.

Meehl, G. A., 1996: Vulnerability of fresh water resources to climate change in the tropical Pacific region. *J. Water Air Soil Pollut.,* **92,** 203–213.

——, 1997: Modification of surface fluxes from component models in global coupled models. *J. Climate,* **10,** 2811–2825.

——, and W. M. Washington, 1993: South Asian summer monsoon variability in a model with doubled atmospheric carbon dioxide concentration. *Science,* **260,** 1101–1104.

——, and ——, 1995: Cloud albedo feedback and the super greenhouse effect in a global coupled GCM. *Climate Dyn.,* **11,** 399–411.

——, and ——, 1996: El Niño-like climate change in a model with increased atmospheric CO_2 concentrations. *Nature,* **382,** 56–60.

——, and J. Arblaster, 1998: The Asian–Australian monsoon and El Niño–Southern Oscillation in the NCAR Climate System Model. *J. Climate,* **11,** 1356–1385.

——, G. W. Branstator, and W. M. Washington, 1993: Tropical Pacific interannual variability and CO_2 climate change. *J. Climate,* **6,** 42–63.

——, W. M. Washington, D. J. Erickson III, B. P. Briegleb, and P. J. Jaumann, 1996: Climate change from increased CO_2 and the direct and indirect effects of sulfate aerosols. *Geophys. Res. Lett.,* **23,** 3755–3758.

——, J. M. Arblaster, and W. G. Strand, 1998: Global scale decadal climate variability. *Geophys. Res. Lett.,* **25,** 3983–3986.

——, ——, and ——, 2000a: Sea ice effects on climate sensitivity and low frequency variability in a global coupled GCM. *Climate Dyn.,* **16,** 257–271.

——, W. Collins, B. Boville, J. T. Kiehl, T. M. L Wigley, and J. M. Arblaster, 2000b: Response of the NCAR Climate System Model to increased CO_2 and the role of physical processes. *J. Climate,* **13,** 1879–1898.

Mitchell, J. F. B., and T. C. Johns, 1997: On modification of global warming by sulfate aerosols. *J. Climate,* **10,** 245–267.

——, ——, J. M. Gregory, and S. F. B. Tett, 1995a: Climate response to increasing levels of greenhouse gases and sulphate aerosols. *Nature,* **376,** 501–504.

——, R. A. Davis, W. J. Ingram, and C. A. Senior, 1995b: On surface temperature, greenhouse gases, and aerosols: Models and observations. *J. Climate,* **8,** 2364–2386.

Noda, A., K. Yamaguchi, S. Yamaki, and S. Yukimoto, 1999: Relationship between natural variability and CO_2−induced warming pattern: MRI AOGCM experiment. Preprints, *10th Symp. on Global Change Studies,* Dallas, TX, Amer. Meteor. Soc., 359–364.

Parker, D. E., M. Jackson, and E. B. Horton, 1995: The GISST2.2 sea surface temperature and sea-ice climatology. Hadley Centre for Climate Prediction and Research, Climate Research Tech. Note 63 (CRTN63), 16 pp. [Available from The Met. Office, London Road, Bracknell, Berkshire RG12 2SY, United Kingdom.]

Parthasarathy, B., K. Rupa Kumar, and A. A. Munot, 1991: Evidence of secular variations in Indian monsoon rainfall–circulation relationships. *J. Climate,* **4,** 927–938.

Rayner, N. A., E. B. Horton, D. E. Parker, C. K. Folland, and R. B. Hackett, 1996: Version 2.2 of the Global Sea-Ice and Sea Surface Temperature data set, 1903–1994. Hadley Centre for Climate Prediction and Research, Climate Research Tech. Note 74 (CRTN74), 21 pp. [Available from The Met. Office, London Road, Bracknell, Berkshire RG12 2SY, United Kingdom.]

Santer, B. D., and Coauthors, 1996: A search for human influences on the thermal structure in the atmosphere. *Nature,* **382,** 39–46.

Tett, S., 1995: Simulation of El Niño–Southern Oscillation-like variability in a global AOGCM and its response to CO_2 increase. *J. Climate,* **8,** 1473–1502.

Timmermann, A., J. Oberhuber, A. Bacher, M. Esch, M. Latif, and E. Roeckner, 1999: ENSO response to greenhouse warming. *Nature,* **398,** 694–697.

Washington, W. M., and G. A. Meehl, 1996: High latitude climate change in a global coupled ocean–atmosphere–sea ice model with increased atmospheric CO_2. *J. Geophys. Res.,* **101,** 12 795–12 801.

Wigley, T. M. L., and S. C. B. Raper, 1990: Natural variability of the climate system and detection of the greenhouse effect. *Nature,* **344,** 324–327.

Zhang, Y., J. M. Wallace, and D. S. Battisti, 1997: ENSO-like decade-to-century scale variability: 1900–93. *J. Climate,* **10,** 1004–1020.